CHAPTER-IV

META-STRUCTURE ABSORBER DEVELOPED EMBEDDING DEEP EUTECTIC SOLVENT GEL

4.1 INTRODUCTION

Permittivity of a material exhibits dispersive behaviour at high frequency operating band, where the ratio of imaginary and real parts of permittivity $\left(\frac{\varepsilon_a''}{\varepsilon_a'}\right)$ indicate the extent of reduction in the amplitude of the interacting EM wave [1, 2]. Slime used in development of MSAs in chapter II and chapter III, shows loss tangent < 1 in X-band. Leveraging ε_a'' will increase the attenuation resulting in enhanced absorption by the MSAs.

Ion combinations of ionic liquids (ILs) contribute an additional conduction loss demonstrating higher microwave absorption [3, 4]. Practical realization of IL based absorbers; however, are limited by its toxic nature and high manufacturing cost. Aqueous electrolytes with NaCl [5-7] and $AlCl_3$ [8] have been investigated as a non-toxic and inexpensive alternative to ILs. The enhanced conduction loss property of electrolytes shows loss tangent values >1 and improve absorption performance [5-8]. There is a threshold of addition of quantity of ionic salt into solution [8], aftermath the loss due to ionic conduction decreases because of ion solvation or hydration sheath formation. Both IL and aqueous electrolytes face fabrication constraints due to their liquid nature as mentioned in chapter I and chapter II.

Investigations conducted to prepare electrolytic gel, alike aqueous electrolyte, by adding ionic salt (NaCl) to slime resulted in breaking of its polymer chains, making it lose its gelated advantage. A similar observation of the slime becoming more liquid-like is observed when instead water, aqueous electrolyte is used during its preparation.

Deep eutectic solvent (DES) is reported to show ionic properties similar to room-temperature ILs [9-16]. These subclass of ILs can be easily gelated with polymerizing agent [14] and have found numerous application in flexible electronics [14, 17, 18]. Additionally, DES has also been used to develop graphene based salisbury screen type absorber in reference [16].

In this chapter, the ionic conductivity property of gelated DES is exploited to develop higher loss subwavelength resonators for fabrication of flexible meta-structure absorber. DES has advantages of low raw material and processing costs, and biodegradability. In line with the previous work conducted in chapter II and III, the

resonators are embedded in silicone rubber. Unit cell is designed and optimized in X-band on CST. Prior to fabrication of MSA, material and microwave characterization of gelated DES are carried out. Absorption performance is evaluated by simulation and verified experimentally. Radar cross section (RCS) performance of the absorber is evaluated and its potential application in RCS reduction is examined.

4.2 PREPARATION AND CHARACTERIZATION OF DEEP EUTECTIC SOLVENT (DES) GEL

Deep eutectic solvents (DES) are usually synthesised by combining a hydrogen bond acceptor (HBA) like ammonium quaternary salt with a metal salt or a hydrogen bond donor (HBD), in an appropriate molar ratio [9-14, 19, 20]. Ethaline is one such DESs which have higher ionic conductivity out of the reported DESs [21] and is chosen for the current work.

4.2.1 Preparation of DES gel

Herein, DES is prepared by mixing choline chloride (ChCl) with formula weight (FW) =139.62 g/mol (Alfa Aesar) which is the HBA and ethylene glycol (EG) of molar mass (M) =62.07 g/mol (Merck's Emparta®) as HBD, in a 1:2 molar ratio, as shown in the schematic, Figure 4.1(a). A transparent and colourless liquid is obtained after continuous stirring of the mixture at temperature about 50-60˚C. Gelation of the DES is carried out by slowly pouring gelatin (Loba Chemie) into it followed by rigorous stirring [22]. The mixture is heated for 2 hours at 70˚C in a hot air oven. A viscous light yellowish liquid is formed. On cooling, the mixture gets gelated as shown in Figure 4.1(b) and (c). Quantity

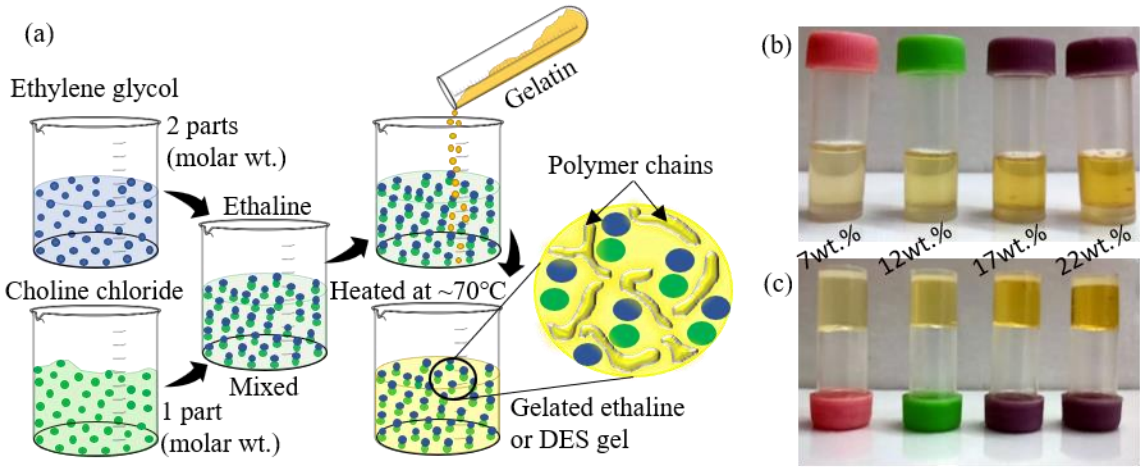

Figure 4.1 (a) Schematic of DES gel preparation. DES gel (b) in sample holders with gelatin 7wt.%, 12wt.%, 17wt.% and 22 wt.% from left and (c) inverted sample holders which confirms gelation of the liquid.

of gelatin in the mixture is varied from 7-22 wt.% in steps of 5. For concentrations beyond 22 wt.% the gel becomes rigid. It is observed that 22 wt.% of gelatin in DES produces a highly viscous gel with good shape retention and elasticity, Figure 4.1(c), and is chosen for further studies (hereafter, termed as DES gel).

4.2.2 Material characterization of DES gel

Some of the in lab characterized material parameters of the DES and DES gel are tabulated in Table 4.1. As inferred from the data in Table 4.1, the DES is conductive (ionic) and the order of magnitude is in agreement with reference [14]. Thermogravimetric analysis (TGA), Figure 4.2(a) of the gel shows a mass loss of ~98% in three step decomposition- (1) 35-195˚C evaporation of water and EG (~35%), (2) 195-250˚C disintegration of amino acids from gelatin disintegrates (~20%) and (3) 250-~500˚C elimination of remaining amino acids and ChCl (~43%). The gel is hydrophilic with contact angles ≪ 90˚, Figure 4.2(b) and can resist high pressure up to 46 kPa beyond which it breaks, Figure 4.2(c). It can regain back its original form (shape/size) on being pressed or stretched (self-healing), Figure 4.2(d).

Table 4.1 Material parameters obtained for the synthesised DES and DES gel.

Material	Material parameter	Values	Equipment/method used
DES (liquid)	Ionic conductivity of DES	9.5 $mScm^{-1}$	InoLab Cond 7110 system
DES gel	Density	1.2645 $g\ cm^{-3}$	Archimedes' principle
DES gel	Decomposition temperature	~37˚C [**Figure 4.2(a)**]	Thermogravimetric analyzer (SHIMADZU-Model: TGA 50)
DES gel	Wettability (Contact angles with water)	≤ 31˚ [**Figure 4.2(b)**]	Contact angle measurement system. (Data physics GmbH, Model: OCA 15 EC)
DES gel	External pressure resistance	≤ 46 kPa [**Figure 4.2(c)** and **(d)**]	$P_{ext} = \frac{\text{Force applied}}{\text{Cross sectional area}}$

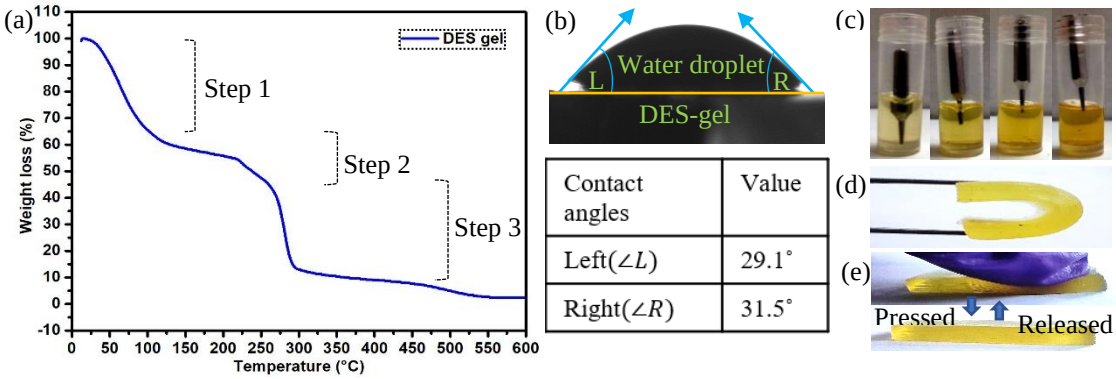

Figure 4.2 Material parameter of DES gel - (a) thermogravimetric analysis plot of DES with 22 wt.% gelatin, (b) contact angles with water, (c) resistance to external pressure by samples with 7wt.%, 12wt.%, 17wt.% and 22 wt.% gelatin from left. (d) The gel is bendable indicating its flexibility and (e) self-healing demonstration.

4.2.3 Microwave characterization of DES gel

The complex permittivity values of the DES gel are characterized by Nicholson-Ross-Weir method detailed in chapter II section 2.5.2 and is plotted in Figure 4.3. High loss tangent is observed of the order of ~1. Prior to measurement rectangular pellets of size 22.86 mm × 10.16 mm × 4.5 mm are made by pouring DES gel liquid into 3D printed moulds for microwave studies as shown in Figure 4.3 inset: (I). Additionally, complex permittivity values of DES are measured and plotted in Figure 4.4(a) and (b) to help understand the loss in the DES gel.

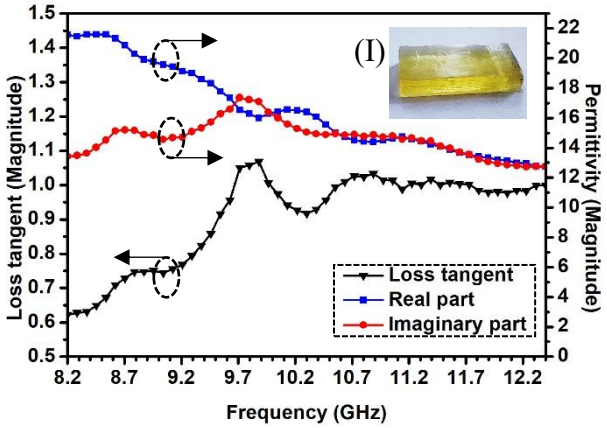

Figure 4.3 Complex permittivity values of DES gel in X-band.

The complex permittivity spectra, Figure 4.4(a) shows that on gelation of DES there is an increase in ε' and with increase in frequency the curve shows downward trend varying from 21.5 to 13.5. The dispersive behaviour could be possibly due to wide range of interactions between the components of the mixture. Unlike atomic and electronic polarization which contributes at IR and visible frequencies, at microwave frequencies orientational (rotational and translational) polarization contributes to complex permittivity. The decreasing dielectric constant is an indication of the phase lag of orientational motion of the dipoles with alternating field and friction between dipoles and charge species at higher frequencies [23]. In DES, the contribution to orientational polarization is from the O-H group of EG (dipolar polarization) and ionic polarization of the delocalised HBA-HBD pairs. In gelated DES, cross linking of gelatin traps the ion in the network resulting in interfacial polarization or Maxwell-Wagner polarization effect [24], hence increasing ε'.

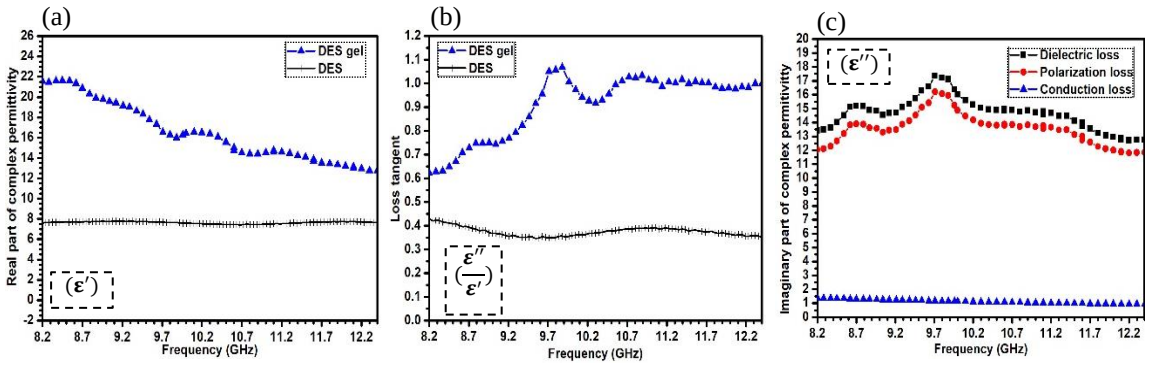

Figure 4.4 (a) Magnitude of real part of permittivity of the DES gel and DES and (b) corresponding loss tangents. Magnitude of imaginary part of permittivity of the DES gel and contributions of polarization and conduction loss.

DES gel shows higher loss tangent ($\varepsilon''/\varepsilon'$) than DES as presented in the plot, Figure 4.4(b). The increasing energy dissipation towards higher frequencies may be attributed to the relaxation phenomenon due to orientational motions of ions and dipoles. The dielectric loss primarily is contribution of polarization loss (dielectric heating) and conduction loss (joule heating) as suggested by Debye's theory [24, 25]. In DES gel, the ionic conductivity also contributes to conduction loss. The Cole–Davidson model (equation (4.1) below) is a modified form of the Debye equation which has been fitted by the permittivity dispersion [26].

$$\varepsilon'' = (\varepsilon_s - \varepsilon_\infty) Cos^{\beta} \beta\omega\tau Sin\beta\omega\tau + \frac{\sigma}{\omega\varepsilon_0} \qquad (4.1)$$

Here, ε_s is the static relative permittivity at low frequencies and ε_∞ is the relative permittivity at high frequencies. ω is the angular frequency of the EM radiation, τ is the relaxation time, σ is the ionic conductivity of the electrolyte (of DES gel inhere which is in the order of $mScm^{-1}$), ε_0 is the permittivity of free space and β is a constant (takes values between 0 and 1) that measures the distribution of relaxation times. The conduction loss is calculated using equation (1) and the contribution of polarization loss is determined by taking the difference of experimental values of ε'' with the conduction loss. The variation of the losses with frequency is placed in Figure 4.4(c). It is evident that polarization loss is dominant in DES gel, however, contribution of conduction loss is also observed.

4.3 DESIGN AND SIMULATION OF DES-GEL-SI-MSA

4.3.1 Design of DES-gel-Si-MSA unit cell

A symmetrical structure gives polarization insensitive absorption as evident from chapter II and chapter III. Here, DES gel is incorporated as four-fold symmetric cuboidal structures in silicone rubber matrix. As in the previous studies conducted a thin layer of silicone rubber is placed on the top of the structure to protect and prevent gel from environmental degradation. The structure is backed by copper. Figure 4.5(a)-(c) shows the schematic of the meta-structure unit cell and the proposed MSA.

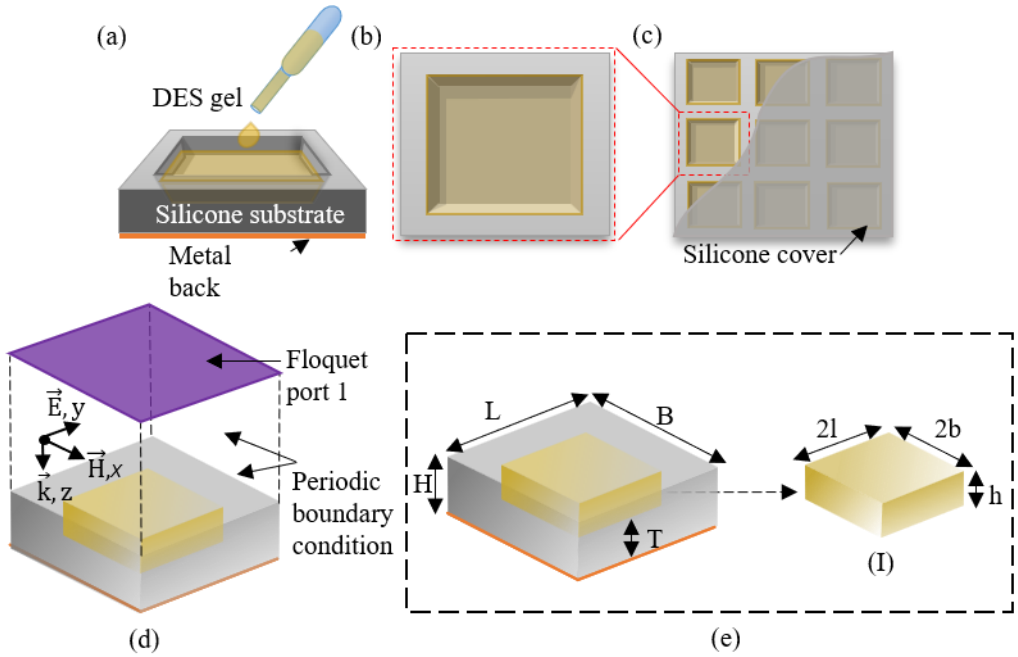

Figure 4.5 Schematic of the proposed MSA unit cell (a) 3D view, (b) top view and (c) periodic arrangement of MSA with silicone rubber cover. (d) A complete simulation set-up with periodic boundaries and Floquet port 1. (e) DES-gel-Si-MSA unit cell's substrate structure and inset (I) the embedded DES gel cuboid.

Table 4.2 Optimized parameters of the DES-gel-Si-MSA.

Structure	Parameter	Magnitude (mm)
Substrate	L=length	8.4
	B=breadth	8.2
	H=height	2.75
	T=thickness of silicone below the DES gel structure	1.0
Top cover	H-T=thickness	0.25
Embedded cuboid	l=length	3.0
	b=breadth	3.0
	h=height	1.5
Copper back	Thickness	0.035

The unit cell dimensions are optimized for minimum reflection and −10 dB absorption bandwidth covering X-band range. Incident directions of electric, magnetic and propagation vectors are shown in Figure 4.5(d). The parameters of the unit cell are illustrated in Figure 4.5(e) and inset: (I) and presented in Table 4.2.

4.3.2 Simulated performance of DES-gel-Si-MSA

The designed MSA (as per specifications given in Table 4.2) resonates at 10.13 GHz at normal incidence with a reflection loss of −39.1 dB and −10 dB absorption bandwidth of ~3.7 GHz, as plotted in Figure 4.6(a). The structure is further simulated at different polarization angles from 0° (co-polarized) to 90° (cross-polarized) with a difference of 30°, Figure 4.6(b). The reflection loss curves overlap for different angles indicating performance to be independent of polarization.

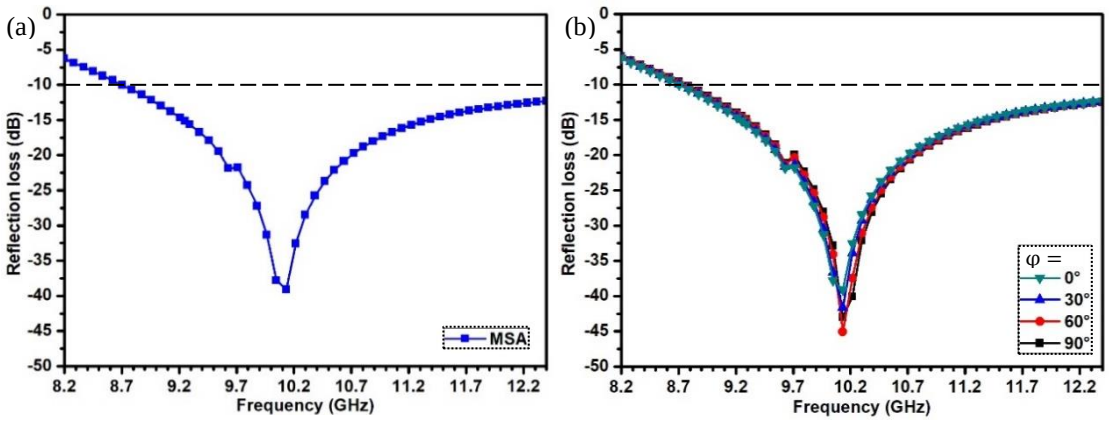

Figure 4.6 Simulated reflection loss of DES-gel-Si-MSA for (a) co-polarization ($\theta = 0, \varphi = 0$) and (b) different polarization angles with $\theta = 0$.

The reflection loss plots in Figure 4.7(a) show dependency on incidence angles. The −10 dB absorption bandwidth is observed to be consistent upto an angle of ±40° for

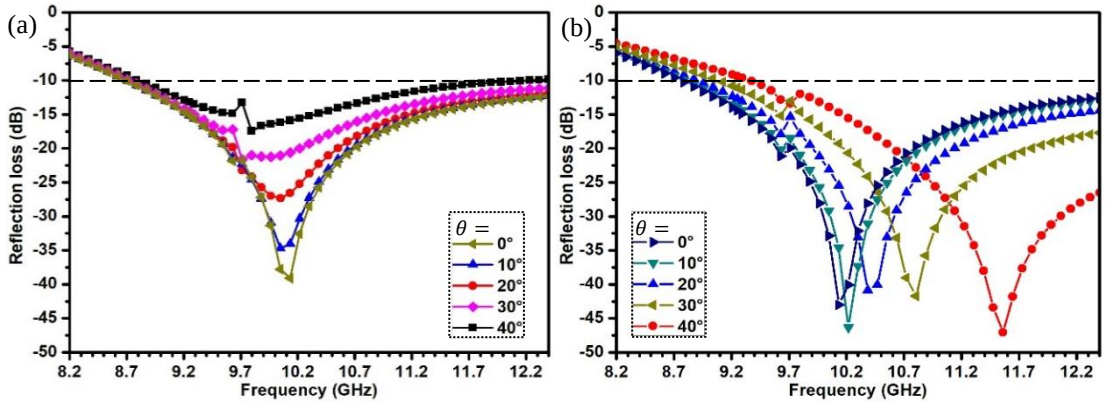

Figure 4.7 Simulated reflection loss of DES-gel-Si-MSA for (a) different incident angles with $\varphi = 0$ in (a) TE mode and (b) TM mode.

TE mode with variation in reflection loss and a minimal shift in resonant frequency, whereas for TM mode, Figure 4.7(b), a shift in resonant frequency and a small shift in -10 dB bandwidth is observed over an angle of $\pm 40^{\circ}$, the reflection loss is < -40 dB for the incident angles studied. The incident electric and magnetic components interact differently with the MSA leading to shift in the reflection loss curves for TE and TM modes.

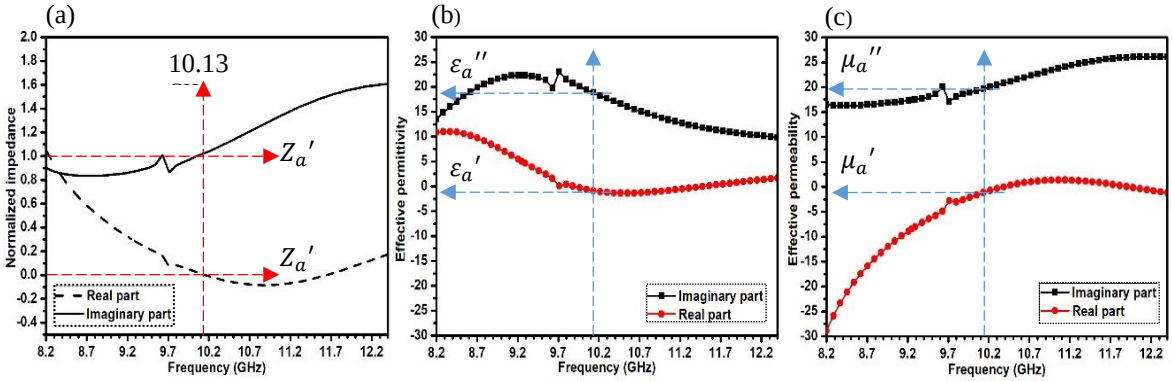

Figure 4.8 Simulated (a) normalized impedance and extracted values of (b) effective permittivity and (c) effective permeability; of DES-gel-Si-MSA.

The real (Z_a')and imaginary part (Z_a'') of the normalized impedance are plotted in Figure 4.8(a). At the resonating frequency, 10.13 GHz, $Z_a' \to 1$ and $Z_a'' \to 0$, where the impedance at the air-absorber interface is matched with the free space. The effective material parameter values can be extracted using the values of impedance (Z_a) and effective refractive index, n given by [27]

$$n = \frac{1}{kd}\cos^{-1}\left[\frac{1}{2S_{21}}(1 - S_{11}^2 + S_{21}^2)\right] \tag{4.2}$$

where, k is the free space wavenumber and d is the thickness of the unit cell. The effective ε_a and μ_a can be determined from the following equations [27]

$$\mu_a = nZ_a \tag{4.3}$$

$$\varepsilon_a = n/Z_a \tag{4.4}$$

The structure behaves as left-handed material at the resonating frequency with effective $\varepsilon_a = -0.88 + \text{j}18.85$ and effective $\mu_a = -1.15 + \text{j}19.66$, refer to Figure 4.8(b) and (c).

Vector distribution analysis are carried out for the E-field and H-field at the resonant frequency. The maximum attenuation of E-field, Figure 4.9(a), is at the edges of the DES gel cuboid. The H-field, Figure 4.9(b), is concentrated at the centre of the DES gel unit and the silicone rubber above the ground surface. The incident H-field component induces current density inside the DES gel, Figure 4.9(c)-(i), and (ii) the loop-shaped currents throughout the DES gel result in induction loss or indirect conduction loss [24]. In addition, the induced currents and the surface currents, Fig Figure 4.9(d), go out of phase resulting in magnetic resonance that further contributes to the effective magnetic permeability of the MSA unit cell.

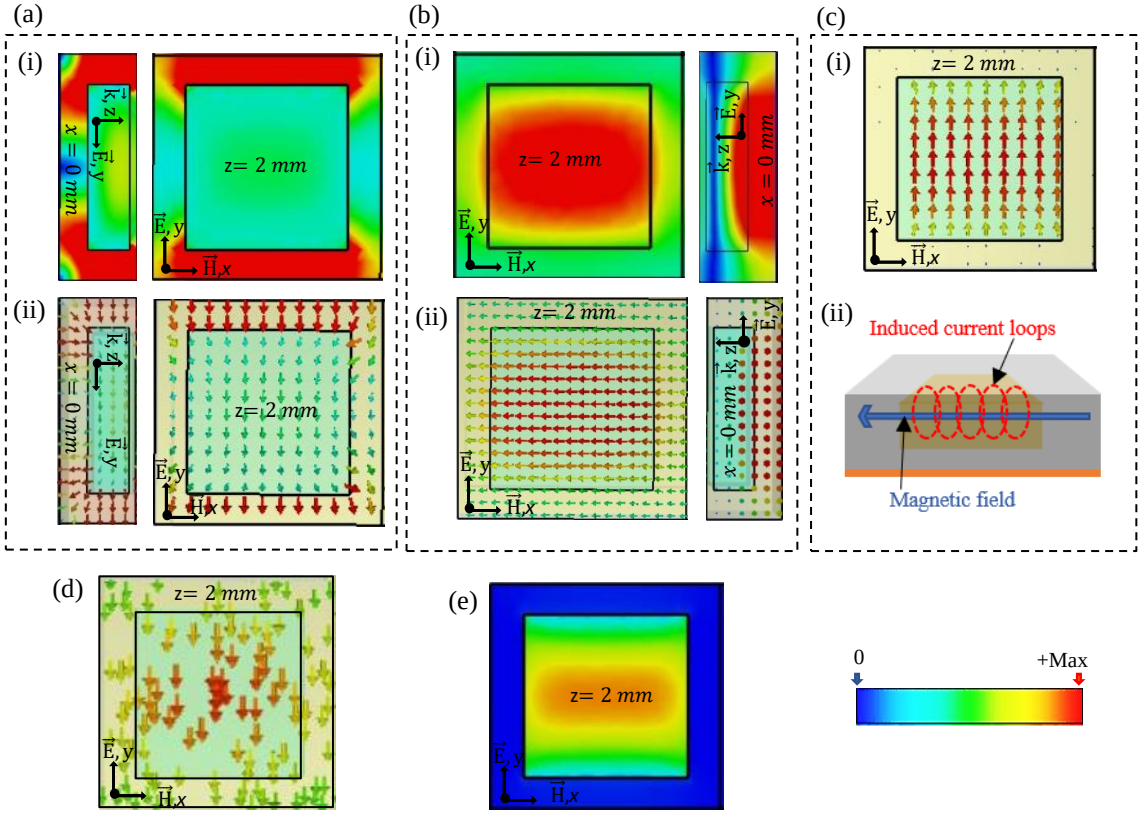

Figure 4.9 (a) Simulated E-field (i) density and (ii) lines of DES-gel-Si-MSA, (b) simulated H-field (i) density and (ii) lines, (c) (i) induced current density and (ii) schematic of induced current loops, (d) surface current on the ground plane and (d) power loss density of DES-gel-Si-MSA, at 10.13 GHz.

The dielectric loss in the gel is mainly due to polarization loss contributed by orientational, ionic, and interfacial polarizations in the gel [20] which couples with the incident E-field component resulting in attenuation as observed in Figure 4.9(e) where the power loss densities is mostly concentrated inside the DES gel.

Structural contribution of MSA can be carried out by comparing the absorption with the proposed unit structure with an equal sized DES gel layer, Figure 4.10(a) and (b). The contribution by DES gel alone to total absorbance is less than 60% implying that localized resonance in the MSA with structured DES gel resonators too contribute to the absorption.

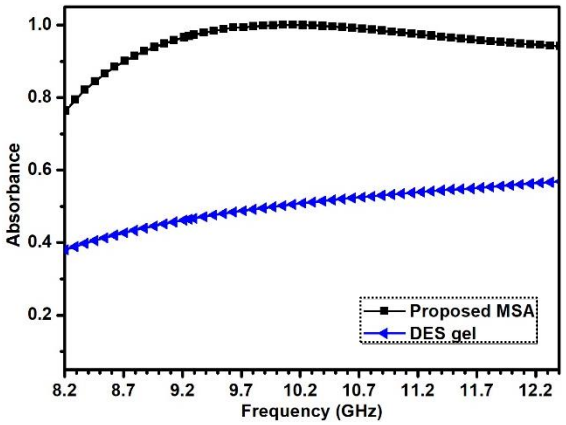

Figure 4.10 Simulated absorbance of DES-gel-Si-MSA and DES gel of same size.

4.4 FABRICATION AND ABSORPTION PERFORMANCE MEASUREMENT

The optimized dimensions, as specified in Table 4.2 are used for fabricating the waveguide sized (22.86 mm × 10.16 mm) MSA which could accommodate two unit cells. Silicone substrate is processed by moulding mixture of liquid silicone rubber and 5 wt% curing agent using additively manufactured moulds developed with BoXZY 3D printer, Figure 4.11(a). The silicone moulds are cured at room temperature for 12 h. The cubical grooves in the substrate are filled with DES gel by slowly dropping the liquid gel at 70°C, Figure 4.11(b). After 12 h, when the gel cools and solidifies sufficiently, silicone rubber is poured to get a cover layer of thickness ~0.25 mm and left undisturbed for another 12 h at room temperature, Figure 4.11(c). The prepared sample is backed with copper tape of thickness ~0.035 mm.

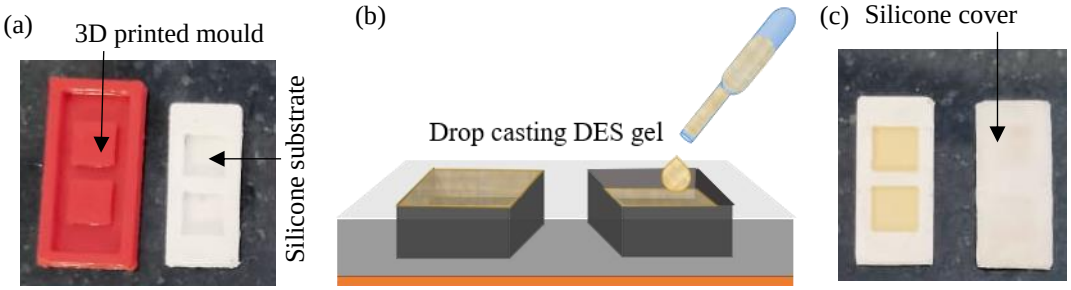

Figure 4.11 (a) Development of the Si substrate, (b) illustration of casting of gel resonators and (c) complete DES-gel-Si-MSA.

The developed MSA's absorption performance is measured using waveguide technique described in chapter II, section 2.5.2 [28]. Experimental and simulated reflection loss curves are depicted in Figure 4.12(a). Corresponding absorbances are plotted in Figure 4.12 (b). Reflection loss is measured to be −38.6 dB at 10.6 GHz, with a −10 dB absorption bandwidth in the range of 9.04 − 12.4 GHz. For a closer approximation to the waveguide technique, simulation is considered for two unit cell structure. The resonant frequency is in closer proximation to the measured result, Figure 4.12(c). Corresponding absorbance also follow the experimental result closely, as obvious from Figure 4.12(d). The results are placed in Table 4.3.

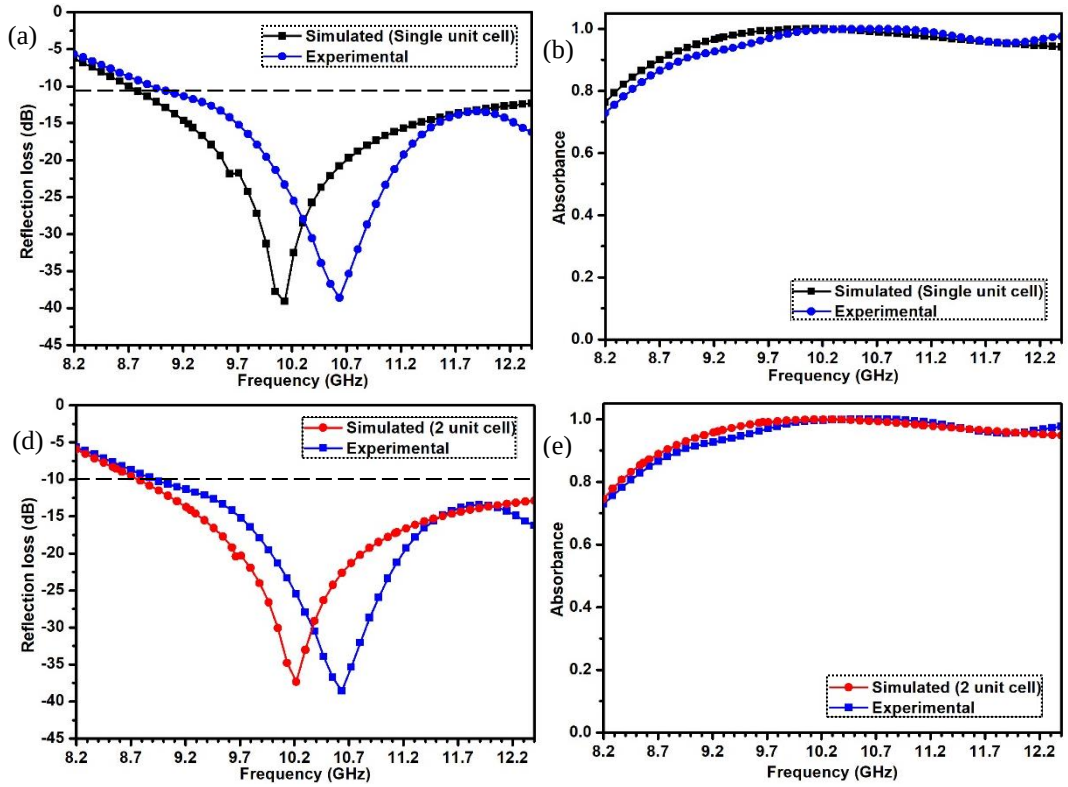

Figure 4.12 Experimental and simulated (single unit cell structure) curves for co-polarized (a) reflection loss and (b) absorbance of DES-gel-Si-MSA. Experimental and simulated (two unit cell structure) curves for co-polarized (c) reflection loss and (d) absorbance of DES-gel-Si-MSA.

Table 4.3 Simulated and measured results.

Absorber	Resonant frequency (GHz)	Reflection loss (dB)	-10 dB Bandwidth (GHz)	% coverage of X-band
Simulated	10.13	-39.1	3.7	88
Experimental	10.6	-38.6	3.36	80

Potential explanations for differences in simulated and experimental resonance frequencies, as well as absorption magnitude, include (1) the waveguide technique

used for measurement has a sample size of $22.86 \times 10.16\ \text{mm}^2$ which can accommodate two unit cells completely leaving the rest as silicone rubber which may alter the material parameter, and (2) fabrication accuracy is considered upto second decimal place which might cause a shift in the results.

4.5 RADAR CROSS SECTION (RCS) EVALUATION

Radar Cross Section (RCS) reduction has long been a challenge where the signature of the target is reduced to non-detectable limits. One of the applied techniques to lower RCS is use of radar absorbing materials either in vicinity of or over the target. Absorbers for RCS applications are expected to have a broad -10 dB absorption bandwidth for a wide angle of incidence and polarization, reduced thickness and lightweight. Other desired requirements are conformability and ease of manufacturing. Embedded meta-structure absorbers (MSAs) are void of metallic resonating structures, which minimize out-of-band reflections reducing the chance of detection by radar systems.

4.5.1 RCS Absorber theory

The radar cross section (RCS) is a crucial metric for determining whether a target has high or poor detectability. It is determined from the target-scattered fields produced when an incident plane wave strikes the target, Figure 4.13. Mathematically, for far-field, RCS in square metres (sm) is expressed as [29, 30]

$$RCS_{(sm)}(\theta, \varphi) = 4\pi \lim_{r \to \infty} r^2 \frac{|E_s(\theta_s, \varphi_s)|^2}{|E_i(\theta_i, \varphi_i)|^2} \tag{4.6}$$

where, r ($r >$far-field) denotes the distance between the radar receiver and the target. E_i is incident electric fields at the target and E_s is the scattered energy received by the receiving antenna Rx. Angles θ_s and φ_s describe the propagation direction of scattered field while, angles θ_i and φ_i describe the propagation direction of incident field. Taking power densities of scattered (PD_s) and incident (PD_i) wave instead, equation (1) transforms to

$$RCS_{(sm)}(\theta, \varphi) = 4\pi \lim_{r \to \infty} r^2 \frac{PD_s(\theta_s, \varphi_s)}{PD_i(\theta_i, \varphi_i)} \tag{4.7}$$

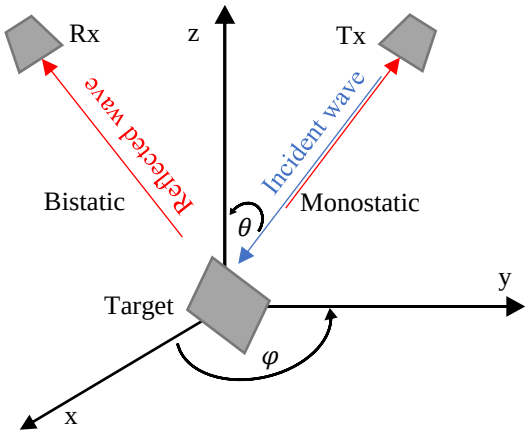

Figure 4.13 Schematic of RCS.

In monostatic RCS, $\theta_s = \theta_i$ and $\varphi_s = \varphi_i$. Writing $PD_s(\theta_s, \varphi_s) = PD_s$ and $PD_i(\theta_i, \varphi_i) = PD_i$, RCS in decibel square metres (dBsm) can be expressed as

$$RCS_{(dBsm)} = 10 \log 4\pi \lim_{r\to\infty} r^2 \frac{PD_s}{PD_i} \tag{4.8}$$

The target's monostatic RCS reduction (RCSR) is found relative to metal as it exhibits maximum reflection upon incidence of plane waves. Hence, monostatic RCS reduction in dB is equivalent to

$$RCSR_{(dB)} = 10\, log \left[\frac{4\pi \lim_{r\to\infty} r^2 \left(\frac{PD_s}{PD_i}\right)_{(Target)}}{4\pi \lim_{r\to\infty} r^2 \left(\frac{PD_s}{PD_i}\right)_{(Metal)}} \right] \tag{4.9}$$

$$\text{Or } RCSR_{(dB)} = 10\, log\, 4\pi \lim_{r\to\infty} r^2 \left(\frac{PD_s}{PD_i}\right)_{(Target)} - 10\, log\, 4\pi \lim_{r\to\infty} r^2 \left(\frac{PD_s}{PD_i}\right)_{(Metal)} \tag{4.10}$$

$$\text{Or} \qquad RCSR_{(dB)} = RCS_{(Target)} - RCS_{(Metal)} \tag{4.11}$$

The target reflects power P_r, which could be related to PD_s by relation $PD_s = P_r/4\pi r^2$ and similarly the incident power could be related to PD_i as $P_i = 4\pi r^2 \times PD_i$. Modified equation (4) in terms of P_r and P_i are

$$RCSR_{(dB)} = 10\, log \left[\frac{4\pi \lim_{r\to\infty} r^2 \left(\frac{P_r}{P_i}\right)_{(Target)}}{4\pi \lim_{r\to\infty} r^2 \left(\frac{P_r}{P_i}\right)_{(Metal)}} \right]$$

$$= 10\, log|R_\omega|_{(Target)} - 10\, log|R_\omega|_{(Metal)} \tag{4.12}$$

where, $|R_\omega|$ is the reflectance. Minimising reflectance of the target will reduce RCS. Inversely, maximizing absorption will reduce RCS. Absorbers dissipate the incident electro-magnetic wave thus reducing scattered wave.

4.5.2 Simulation of RCS of DES-gel-Si-MSA

RCS simulation is carried out using CST for the DES-gel-Si-MSA sized as $15\text{ cm} \times 15\text{ cm} = 5\lambda \times 5\lambda$ with $19 \times 19 = 361$ unit cells. Studies are conducted with reference to same-sized copper plate. Both bistatic and monostatic simulations are carried out for co- and cross-polarizations. Figure 4.14(a) shows the 3-D bistatic RCS, it can be observed that the maximum RCS value for copper plate is ~9 dB whereas the MSA shows a maximum RCS value of ~ -19 dB. Figure 4.14(b) and Figure 4.14(c) plots, respectively, bistatic RCS for co-polarized ($\varphi = 0°$) and cross-polarized ($\varphi = 90°$) incident wave at different incidence angle, theta (θ). It can be inferred that the DES-gel-Si-MSA reduces RCS almost to 20 dB for $\theta = \pm 40°$.

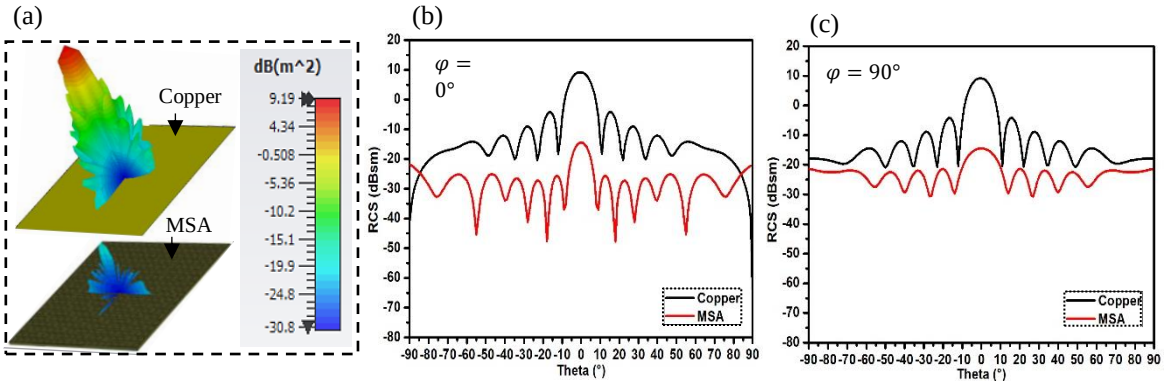

Figure 4.14 Simulated bistatic RCS plots of copper and DES-gel-Si-MSA- (a) 3-D representation, (b) co-polarization and (c) cross-polarization.

Monostatic RCS reduction is determined from the equation (4.11) which can be modified as below with a change in polarity of the resultant values

$$RCSR_{(dB)} = RCS_{(Copper)} - RCS_{(MSA)} \tag{4.13}$$

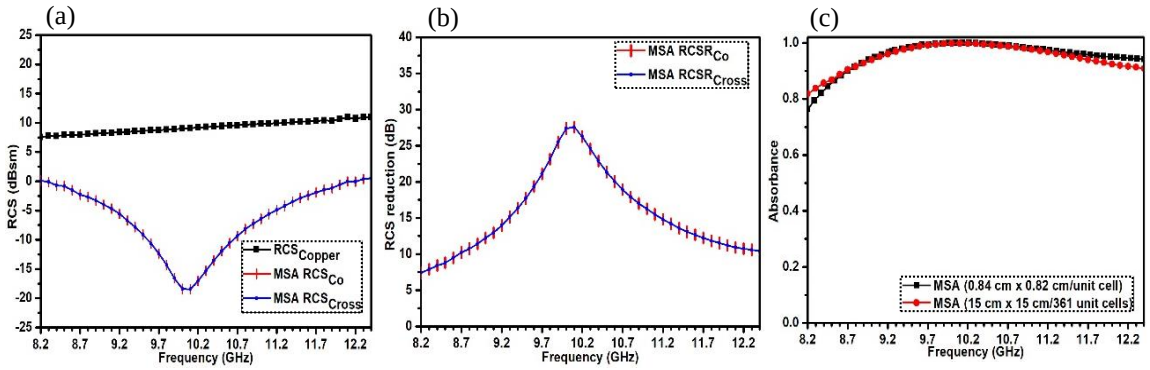

Figure 4.15 (a) Simulated co- and cross-polarized monostatic RCS plots of copper and DES-gel-Si-MSA, (b) co- and cross-polarized monostatic RCS reduction in DES-gel-Si-MSA with reference to copper, (c) co-polarized absorbance curves for simulated unit cell structure (0.84 cm × 0.82 cm) and DES-gel-Si-MSA with 361 unit cells (15 cm × 15 cm).

Monostatic co-polarized and cross-polarized RCS values for MSA and copper is given in Figure 4.15(a). The monostatic RCS reduction estimated using equation (4.13) are plotted in Figure 4.15(b). A reduction of more than 25 dB is observed at the resonant frequency showing a 10 dB RCS bandwidth of 3.73 GHz. Figure 4.15(c) plots corresponding absorbance using equations (4.12) and (1.2). Absorbance of single simulated unit cell using Floquet port is plotted along with and a good agreement with the far-field simulation is observed.

4.5.3 Measurement of monostatic RCS of DES-gel-Si-MSA

Monostatic RCS measurement set-up schematic is given in Figure 4.16(a). A transmitting antenna (Tx) and receiving antenna (Rx) are placed almost co-sited. The target is placed at far-field (> 60 cm). The measurement is carried out in two stages - Measuring reflectance of 1. PEC and 2. PEC covered with the absorber [31]. Here a 15 cm × 15 cm copper plate is taken as PEC and later covered by fabricated DES-gel-Si-MSA of the same dimension (Figure 4.16(b)). The in-lab developed measurement set-up is shown in Figure 4.16(c). Directive Aaronia antennas (HyperLOG60200X) are used as Tx and Rx. Reflectance is measured using Anritsu MS46322B VNA. The monostatic RCS for both co- and cross-polarized incidence is measured and plotted.

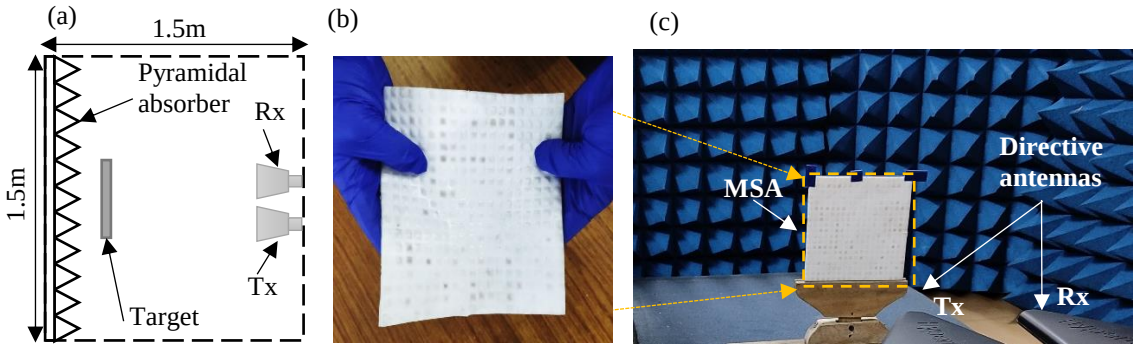

Figure 4.16 (a) Schematic of RCS measurement set-up. (b) Developed DES-gel-Si-MSA (15 cm × 15 cm sample) and (c) In-lab measurement set-up.

Measured monostatic RCS values of copper and the developed MSA for both co-polarized and cross-polarized incidence are shown in Figure 4.17(a). RCS reduction ≥ 10 dB for both co-and cross-polarization in reference to copper is observed for almost 80% of X-band, Figure 4.17(b). On comparing the experimental results with the simulated (Figure 4.17(c)) the 10 dB RCS bandwidth is found to be in good agreement. The variation in the RCS values could be possibly due to some near-field

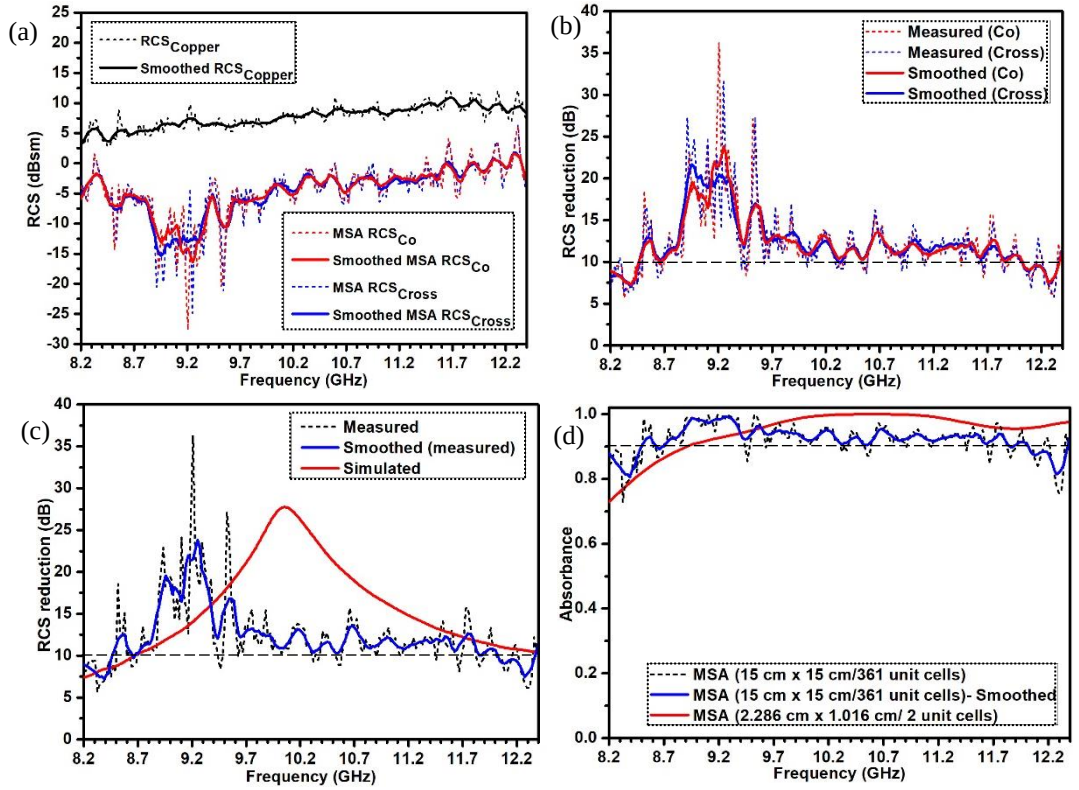

Figure 4.17 (a) Measured monostatic RCS of copper and MSA (both co-polarized and cross-polarized incidence), (b) measured monostatic RCSR of MSA for both co-polarized and cross-polarized incidence, (c) measured and simulated RCSR values for co-polarized incidence and (d) measured co-polarized absorbance in DES-gel-Si-MSA for far-field and waveguide technique.

interference caused by the close proximity of Tx and Rx antennas in the experimental arrangement. The material parameters used for simulation are generally rounded off which may result in a shift of the reduction peak and moreover, there is always a limit to fabrication accuracy. In line with the absorbance determined for simulation (Figure 4.15(c)), absorbance determined using measured RCS reduction for 361 unit cells (far-field technique) is plotted in Figure 4.17(d) alongwith the absorbance of MSA with two unit cells measured using waveguide technique. The measured absorbance showed 90% absorption in the range of $8.45 - 12$ GHz while simulated is showing an absorption in the range $8.9 - 12.4$ GHz. The small dissimilarity observed could have resulted because of the edge diffraction. From the studies conducted, it can be inferred that good absorbers can effectively lower RCS.

4.6 CHAPTER SUMMARY

A meta-structure absorber is designed and fabricated using pliable silicone rubber wherein DES gel is infused in cuboidal grooves. Gel and the silicone rubber in

combination make the MSA flexible. The high permittivity loss tangent of the gel helps to achieve a better impedance matching at the air-absorber covering more than 80% of the X-band with single resonator. The periodicity and overall thickness of the DES-gel-Si-MSA reduced compared to slime based MSAs. The four-fold symmetry of the embedded gel resonator assists in polarization insensitive RCS performance. The measured findings show that the DES-gel-Si-MSA can effectively lower the RCS to more than 10 dB (in reference to the metal plate) over a bandwidth of 3.55 GHz (~35%) of X-band. The summary of the developed DES-gel-Si-MSA's specifications are tabulated in Table 4.4.

Table 4.4 Summary of DES-gel-Si-MSA's specifications.

Result→	*Measured*								*Simulated*	
Parameter	**RF (GHz)**	**RL (dB)**	**% coverage of X-band**	**10 dB RCSR BW (GHz)**	**Thickness**	**WA (%)**	**ρ (g cm^{-3})**	**P: L & B (mm)**	**PA-T**	**IA-T**
Values	10.6	-38.6	>80	8.45-12	2.75 ($0.0775\lambda_0$)	0.6	~1.2	8.4 × 8.2	±90°	±40°
Note: RF- Resonant frequency, RL-reflection loss, BW- bandwidth $\boldsymbol{\lambda_0}$-lowest operating frequency, WA-water absorbance, **ρ**- density, P-periods: L- length and B- breadth of MSA unit cell, PA-T- polarization angle tolerance, IA-T-incidence angle tolerance.										

REFERENCES

[1] Baker-Jarvis, J. and S. Kim, The interaction of radio-frequency fields with dielectric materials at macroscopic to mesoscopic scales*. Journal of research of the National Institute of Standards and Technology*, 117: 1, 2012.

[2] Sun, J., W. Wang, and Q. Yue, Review on microwave-matter interaction fundamentals and efficient microwave-associated heating strategies*. Materials*, 9(4): 231, 2016.

[3] Tang, J., M. Radosz, and Y. Shen, Poly (ionic liquid) s as optically transparent microwave-absorbing materials*. Macromolecules*, 41(2): 493-496, 2008.

[4] Yang, F., et al., Microwave-absorbing properties of room-temperature ionic liquids*. Journal of Physics D: Applied Physics*, 52(15): 155302, 2019.

[5] Peyman, A., C. Gabriel, and E. Grant, Complex permittivity of sodium chloride solutions at microwave frequencies*. Bioelectromagnetics: Journal of the Bioelectromagnetics Society, The Society for Physical Regulation in Biology and Medicine, The European Bioelectromagnetics Association*, 28(4): 264-274, 2007.

[6] Nörtemann, K., J. Hilland, and U. Kaatze, Dielectric properties of aqueous NaCl solutions at microwave frequencies*. The Journal of Physical Chemistry A*, 101(37): 6864-6869, 1997.

[7] Xiong, H. and F. Yang, Ultra-broadband and tunable saline water-based absorber in microwave regime*. Optics Express*, 28(4): 5306-5316, 2020.

[8] Gogoi, D.J. and N.S. Bhattacharyya, Microwave metamaterial absorber based on aqueous electrolyte solution for X-band application*. Journal of Applied Physics*, 125(12), 2019.

[9] Smith, E.L., A.P. Abbott, and K.S. Ryder, Deep eutectic solvents (DESs) and their applications*. Chemical reviews*, 114(21): 11060-11082, 2014.

[10] Pandey, A., et al., How polar are choline chloride-based deep eutectic solvents? *Physical Chemistry Chemical Physics,* 16(4): 1559-1568, 2014.

[11] Vanda, H., et al., Green solvents from ionic liquids and deep eutectic solvents to natural deep eutectic solvents*. Comptes Rendus Chimie*, 21(6): 628-638, 2018.

[12] Roda, A., et al., Polymer science and engineering using deep eutectic solvents. *Polymers*, 11(5): 912, 2019.

[13] Nahar, Y. and S.C. Thickett, Greener, Faster, Stronger: The Benefits of Deep Eutectic Solvents in Polymer and Materials Science. *Polymers*, 13(3): 447, 2021.

[14] Bu, X., et al., Design of highly stretchable deep eutectic solvent-based ionic gel electrolyte with high ionic conductivity by the addition of zwitterion ion dissociators for flexible supercapacitor. *Polymer Engineering Science,* 61(1): 154-166, 2021.

[15] Sekharan, T.R., et al., Deep eutectic solvents as an alternate to other harmful solvents. *Review*, 2022(12): 847-860, 2022.

[16] Grande, M., et al., Reconfigurable and optically transparent microwave absorbers based on deep eutectic solvent-gated graphene. *Scientific reports*, 9(1): 1-9, 2019.

[17] Zhang, P., et al., Natural deep eutectic solvent-based gels with multi-site interaction mechanism for selective membrane separation of SO2 from N2 and CO2. *Chemical Engineering Journal*, 438: 135626, 2022.

[18] Chen, T.-Y., Y.-J. Jiang, and H.-W. Chien, Developing Transparent and Conductive PolyHEMA Gels Using Deep Eutectic Solvents. *Polymers*, 15(12): 2605, 2023.

[19] Leleux, P., et al., Ionic Liquid Gel-Assisted Electrodes for Long-Term Cutaneous Recordings. *Advanced healthcare materials*, 3(9): 1377-1380, 2014.

[20] Wang, H., et al., Ionic gels and their applications in stretchable electronics. *Macromolecular rapid communications*, 39(16): 1800246, 2018.

[21] Reuter, D., et al., Ionic conductivity of deep eutectic solvents: The role of orientational dynamics and glassy freezing. *Physical Chemistry Chemical Physics*, 21(13): 6801-6809, 2019.

[22] Delbecq, F., et al., Study of a gelated Deep Eutectic solvent metal salt solution as template for the production of size-controlled small noble metal nanoparticles. *Colloids Surfaces A: Physicochemical Engineering Aspects,* 567: 55-62, 2019.

[23] Barthel, J., et al., Molecular processes in electrolyte solutions at microwave frequencies*. Pure and applied chemistry*, 62(12): 2287-2296, 1990.

[24] Horikoshi, S., T. Sumi, and N. Serpone, Unusual effect of the magnetic field component of the microwave radiation on aqueous electrolyte solutions*. Journal of Microwave Power Electromagnetic Energy,* 46(4): 215-228, 2012.

[25] Barthel, J., et al., Molecular processes in electrolyte solutions at microwave frequencies*.* 62(12): 2287-2296, 1990.

[26] Liu, P.-B., Y. Huang, and X. Sun, Excellent electromagnetic absorption properties of poly (3, 4-ethylenedioxythiophene)-reduced graphene oxide–Co3O4 composites prepared by a hydrothermal method*. ACS applied materials & interfaces*, 5(23): 12355-12360, 2013.

[27] Smith, D., et al., Electromagnetic parameter retrieval from inhomogeneous metamaterials*. Physical review E*, 71(3): 036617, 2005.

[28] Rothwell, E.J., et al., Analysis of the nicolson-ross-weir method for characterizing the electromagnetic properties of engineered materials*. Progress In Electromagnetics Research*, 157: 31-47, 2016.

[29] Knott, E.F., J.F. Schaeffer, and M.T. Tulley Radar cross section. SciTech Publishing, 2004.

[30] Mahafza, B.R. Radar systems analysis and design using MATLAB. CRC press, 2022.

[31] Nowosielski, L., et al., The Absorption Capability Measurements of the Free Space Absorbers*. PIERS Online*, 6(1): 86-90, 2010.